

Dartmouth College

Dartmouth Digital Commons

Dartmouth Scholarship

Faculty Work

12-1-2021

Visualizing temperature-dependent phase stability in high entropy alloys

Daniel Evans

University of Michigan, Ann Arbor

Jiadong Chen

University of Michigan, Ann Arbor

George Bokas

Université Catholique de Louvain

Wei Chen

Université Catholique de Louvain

Geoffroy Hautier

Université Catholique de Louvain

See next page for additional authors

Follow this and additional works at: <https://digitalcommons.dartmouth.edu/facoa>

Dartmouth Digital Commons Citation

Evans, Daniel; Chen, Jiadong; Bokas, George; Chen, Wei; Hautier, Geoffroy; and Sun, Wenhao, "Visualizing temperature-dependent phase stability in high entropy alloys" (2021). *Dartmouth Scholarship*. 4128. <https://digitalcommons.dartmouth.edu/facoa/4128>

This Article is brought to you for free and open access by the Faculty Work at Dartmouth Digital Commons. It has been accepted for inclusion in Dartmouth Scholarship by an authorized administrator of Dartmouth Digital Commons. For more information, please contact dartmouthdigitalcommons@groups.dartmouth.edu.

Authors

Daniel Evans, Jiadong Chen, George Bokas, Wei Chen, Geoffroy Hautier, and Wenhao Sun

ARTICLE OPEN



Visualizing temperature-dependent phase stability in high entropy alloys

Daniel Evans¹, Jiadong Chen¹, George Bokas², Wei Chen², Geoffroy Hautier^{2,3} and Wenhao Sun¹✉

High entropy alloys (HEAs) contain near equimolar amounts of five or more elements and are a compelling space for materials design. In the design of HEAs, great emphasis is placed on identifying thermodynamic conditions for single-phase and multi-phase stability regions, but this process is hindered by the difficulty of navigating stability relationships in high-component spaces. Traditional phase diagrams use barycentric coordinates to represent composition axes, which require $(N - 1)$ spatial dimensions to represent an N -component system, meaning that HEA systems with $N > 4$ components cannot be readily visualized. Here, we propose forgoing barycentric composition axes in favor of two energy axes: a formation-energy axis and a 'reaction energy' axis. These Inverse Hull Webs offer an information-dense 2D representation that successfully captures complex phase stability relationships in $N \geq 5$ component systems. We use our proposed diagrams to visualize the transition of HEA solid-solutions from high-temperature stability to metastability upon quenching, and identify important thermodynamic features that are correlated with the persistence or decomposition of metastable HEAs.

npj Computational Materials (2021)7:151 | <https://doi.org/10.1038/s41524-021-00626-1>

INTRODUCTION

Traditional alloy design consists of one or two principal elements alloyed with small amounts of supplementary elements. On the other hand, high entropy alloys (HEAs) contain near equimolar amounts of five or more elements and offer promising mechanical behavior^{1–5}, corrosion resistance^{6,7}, and compositional tunability^{8,9}. Additionally, high-component ceramics^{10–13} can be semiconductors^{14,15} or used as cathodes in Li-ion batteries^{16,17}, illustrating the promise of entropy-stabilized materials. A large number of compositional degrees of freedom available in the search for high-component materials gives rise to an exciting and still largely unexplored materials design space¹⁸. So far, significant emphasis has been placed on identifying the single-phase and multi-phase equilibrium regions in an HEA phase diagram^{19–22}—where a single-phase HEA is defined by random mixing of all atoms on the same lattice in a homogeneous solid-solution. Thermodynamically, this single-phase HEA solid-solution will be stable if it is lower in free energy than any linear combination of its lower-component ordered intermetallics and solid-solutions.

Unfortunately, there is a lack of suitable tools to visualize thermodynamic competition in high-component chemical spaces, which impedes the guided exploration of HEAs. Traditional phase diagrams use barycentric composition axes, where compound compositions are given by the lever rule. A barycentric representation of an N -component system requires $D = (N - 1)$ spatial dimensions, meaning systems with $N \geq 5$ components cannot be visualized in $D \leq 3$ spatial dimensions. Past attempts to visualize HEA stability include projecting a five-component phase diagram into three dimensions, or constructing a series of quaternary phase diagrams²³. However, these approaches do not scale to an arbitrary number of components, and do not quantitatively display relative thermodynamic relationships between phases—especially as a function of temperature. Developing a scheme to visualize stability relationships in high-

component systems would help facilitate the discovery of promising HEA compositions.

Here, we propose an information-dense^{24,25} 2D representation that captures the essence of phase stability relationships in high-component systems while remaining easily interpretable. We choose to forgo barycentric composition axes in order to avoid the scaling relationship between components and dimensions; and instead adopt a graph-based representation of stability relationships. However, unlike previous graph-based stability representations, which do not have meaningful x and y -axes^{26,27}, we assign a formation energy axis and a reaction energy axis, capturing the absolute and relative stabilities of competing N -component phases. Furthermore, we design a variety of plot features including color, line-width, and marker shape to retain salient compositional information lost by eliminating barycentric composition axes.

We name these diagrams Inverse Hull Webs and use them to illustrate temperature-dependent phase-stability during the quenching of HfMoNbTiZr and AlCrFeNi, which are experimentally reported to be a single-phase and a multiphase HEA system, respectively. Our Inverse Hull Webs capture high-level trends in HEA solid-solution stability, as well as precise thermodynamic details regarding phase decomposition across the HEA composition space. Additionally, by animating our diagrams as a function of temperature, we can track the transition of an HEA solid-solution from stability to metastability upon cooling and identify which intermetallic compounds threaten phase separation in the HEA solid-solution phase. Finally, we identify two features from our Inverse Hull Webs that indicate the propensity of an HEA either to persist as a single-phase solid-solution at room temperature or to phase separate—and validate these features to have high classification accuracy against a dataset of 103 experimentally-characterized HEAs.

More broadly speaking, our use of energy axes allows our Inverse Hull Webs to offer a complementary perspective to

¹Department of Materials Science and Engineering, University of Michigan, Ann Arbor, MI, USA. ²Institute of Condensed Matter and Nanosciences (IMCN), UCLouvain, Louvain-La-Neuve, Belgium. ³Thayer School of Engineering, Dartmouth College, Hanover, NH, USA. ✉email: whsun@umich.edu

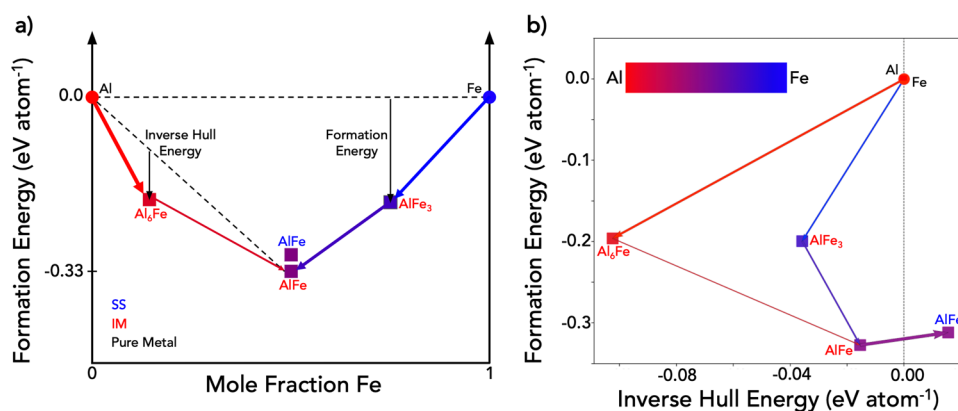


Fig. 1 Conversion of the convex hull to Inverse Hull Web. **a** Convex Hull of Al–Fe system at 1250 K, with formation energy on the y -axis and mole fraction Fe on the x -axis. The dotted line connecting Al and AlFe demonstrates the process for finding Al₆Fe’s hull reactants and inverse hull energy. The arrow width representation of phase fraction is shown as the arrow connecting Al₆Fe to Al is thicker than the arrow connecting Al₆Fe to AlFe. **b** Inverse hull web of Al–Fe system at 1250 K, with formation energy on the y -axis and inverse hull energy on the x -axis. The AlFe solid-solution lies to the right of the dotted line, indicating it is metastable with respect to an AlFe intermetallic. The code used to generate Inverse Hull Webs can be found in Supplementary Data 1.

traditional phase diagrams, highlighting important thermodynamic features that are typically missing from traditional phase diagrams such as convex hull depth, reaction driving forces, metastability, and the tendency for phase separation. Our visualization is therefore useful for generally understanding materials stability, including in ordered, low-component materials systems. Beyond Inverse Hull Webs, we believe that there may exist many creative ways to visualize phase stability relationships, which can serve as theoretical tools to discover and design advanced materials.

RESULTS

Design of inverse hull webs

Phase stability is governed by the convex hull construction, as illustrated in Fig. 1a. By plotting the formation energy of materials against composition, the stable phases lie on the lower convex hull formed between compounds and their elemental reference states²⁸. Thermodynamically stable phases are vertices on the convex hull, while metastable phases have an energy above the convex hull at their associated composition²⁹. Phase coexistence occurs when a point lies on a facet, or simplex, of the convex hull. The convex hull of an N -component system is plotted in a barycentric representation in $(N - 1)$ dimensions. The scaling relationship between the number of components, N , and the number of spatial dimensions, D , is the source of the difficulty in visualizing stability relationships in high-component systems. Notably, a five-component convex hull would need to be visualized in four spatial dimensions.

Here, we propose a 2D visualization scheme, which we name *Inverse Hull Webs*, that captures important information from the thermodynamic convex hull and does not use barycentric composition axes, meaning that our diagrams are not spatially constrained by the number of components in the system. Figure 1b illustrates the conversion of a traditional convex hull to our Inverse Hull Webs for the binary Al–Fe system at 1250 K. We construct Fig. 1 using DFT-calculated 0 K formation enthalpies of pure metals and intermetallic phases and the 1250 K regular solution free energy of the AlFe solid-solution, as described in the “Methods” section.

We use formation energy on the y -axis and *inverse hull energy* on the x -axis of our Inverse Hull Webs. Formation energy is the free energy difference between a phase and the linear combination of its corresponding pure elements, as noted in Fig. 1a by an arrow for AlFe₃. In the computational materials design community,

it is conventional to define energies relative to the convex hull; a stable phase has $\Delta E_{\text{hull}} = 0$ and metastable phases have an energy ‘above the hull’, which is the difference in formation energy between a metastable phase and its stable decomposition products²⁹. Here, we generalize this concept—defining the inverse hull energy to be the reaction energy to a phase from its stable neighbors in composition space—which we call the hull reactants. In other words, the inverse hull energy for a metastable phase is simply its ‘energy above the hull’, but for a stable phase, it is the energy below a hypothetical convex hull where the stable phase was removed, as illustrated for Al₆Fe in Fig. 1a. Stable and metastable phases can be quickly identified on an Inverse Hull Web, as they fall to the left or right of zero inverse hull energy (shown on the figure as 0 on the x -axis), respectively. We note that metastable phases are not shown on traditional triangular and tetrahedral phase diagrams. Additionally, our Inverse Hull Webs provide the same information regarding metastable phases as binary and ternary convex hulls, namely the energy of the metastable phase along with its composition. The equations used to calculate the formation energy of AlFe₃ and the inverse hull energy of Al₆Fe in Fig. 1a can be found in Eqs. 1 and 2, respectively.

$$\Delta G_{\text{form}}^{\text{AlFe}_3} = G^{\text{AlFe}_3} - \frac{1}{4}(G^{\text{Al}} + 3G^{\text{Fe}}) \quad (1)$$

$$\Delta G_{\text{IHE}}^{\text{Al}_6\text{Fe}} = \Delta G_{\text{form}}^{\text{AlFe}_3} - \frac{1}{7}(5\Delta G_{\text{form}}^{\text{Al}} + \Delta G_{\text{form}}^{\text{AlFe}}) \quad (2)$$

By eliminating barycentric axes, we lose important information regarding the composition of the phases. We design a variety of plot features—such as arrows, arrow width, marker shape, and color—to regain this compositional information. First, we use arrows to connect hull reactants to product phases, based on the inverse hull energy definition. We emphasize that these arrows do not represent tie lines, for example as was used by Hegde et al.²⁶ in their phase stability network representation. While tie lines visualize two-phase coexistence, our arrows indicate reactions between compositional neighbors on the convex hull. This distinction becomes clear in $N \geq 3$ component systems, as the ‘hull reactants’ are not necessarily the phases connected to a compound by its tie lines. Supplementary Fig. 1 in the Supplementary Note can be referred to for a visualization of the difference between the hull reactants of a ternary compound and the phases it is connected to by tie lines.

We retain the coefficients of a stoichiometrically-balanced reaction by using arrow widths to represent the phase fraction of each hull reactant, where thicker arrows correspond to larger

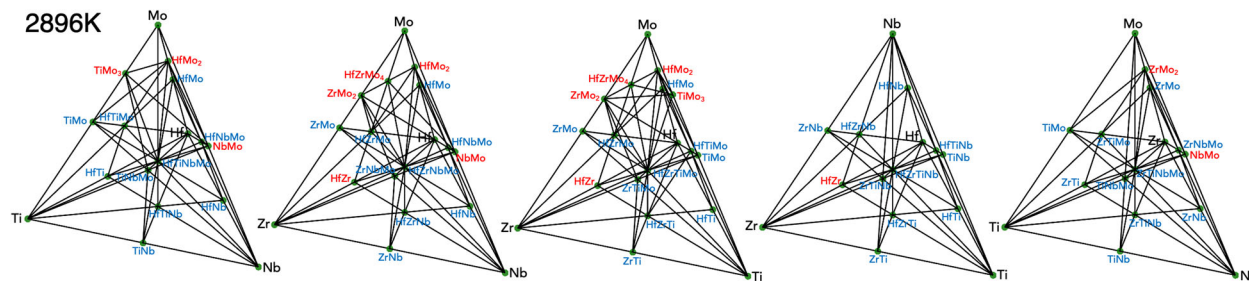


Fig. 3 Phase diagram of the Hf–Mo–Nb–Ti–Zr system. A series of quaternary phase diagrams representing the Hf–Mo–Nb–Ti–Zr system. Stable phases are indicated by green points on the tetrahedra. Intermetallic phases are labeled in red text while solid solution phases are labeled in blue. The diagrams are constructed at 2896 K, the melting temperature of pure Mo.

favoured over solid-solutions with high configurational entropy. This means that many single-phase HEAs may be metastable at room temperature relative to these ordered lower-component intermetallics. Thus, many single-phase HEAs should be temperature-stabilized somewhere between room temperature and the melting point of the alloy.

We will use our Inverse Hull Webs to visualize the transition of an HEA solid-solution from stability to metastability as it is quenched and illustrate how it can be used to guide the design of compelling HEA compositions. We will examine two HEAs: HfMoNbTiZr, which was experimentally reported to be single-phase HEA when quenched; and AlCrFeNi, which phase-separates upon quenching. In our analysis, the only metastable phases we consider are solid-solution phases, and not metastable intermetallics. We display Inverse Hull Webs of these systems at a series of representative temperatures during quenching. Additionally, we have included Python code and a Jupyter notebook in Supplementary Data 1 which can be used to generate these Inverse Hull Webs. We have also included Inverse Hull Webs of 103 equimolar, as-cast HEAs listed in³⁶ in Supplementary Data 2. Users can zoom into the Inverse Hull Webs when using the Python code, elucidating crowded areas of the diagram.

Inverse hull web of an experimentally-observed single-phase HEA

Here, we examine HfMoNbTiZr, an HEA that Tseng et al. found to be a single BCC solid-solution phase at room temperature after being cast through vacuum arc melting and remelted at least four times³⁷. First, we present a visualization of phase stability in this system using traditional phase diagrams, as shown in Fig. 3. This appears as a series of tetrahedral phase diagrams, one for each of the four-element combinations found in Hf–Mo–Nb–Ti–Zr. These phase diagrams are calculated at 2896 K, the highest melting temperature of the pure elements in the system.

In this traditional phase diagram representation, the HEA solid-solution phase is not present in Fig. 3, as a five-component compound cannot be shown on a tetrahedral phase diagram. There are many tie lines present on each of the tetrahedral diagrams, and the 3D aspect of the diagrams means that many of these tie lines overlap. This makes it difficult to discern the multiphase regions and obfuscates the use of barycentric coordinates to evaluate phase fractions by the lever rule.

In contrast, the Inverse Hull Web of HfMoNbTiZr is shown in Fig. 4 at four important temperatures during a quenching process; first, at the Mo melting temperature, 2896 K; and lastly, at room temperature, 300 K. Our Inverse Hull Webs offer a complement to the traditional phase diagram visualization, as we are able to clearly display the relative energy and hull reactants of each of the phases, features not found in Fig. 3. We also show the Inverse Hull Web at two critical temperatures that we have identified during quenching.

We call the first critical temperature the ‘critical solid-solution’ temperature, or the lowest temperature where the HEA solid-solution is stable, which is 563 K in this system. This temperature represents where the HEA solid-solution becomes metastable during quenching, giving insight into the likelihood the alloy will be found as a single phase at room temperature. This temperature also represents the critical miscibility temperature of the HEA solid-solution, where below the ‘critical solid-solution’ temperature, at least one element is no longer fully miscible in the HEA lattice. The next critical temperature we consider is the alloy’s ‘critical adjacent phase’ temperature, or the lowest temperature where the N -component HEA solid-solution phase’s hull reactants are all of the compositionally-adjacent, $(N - 1)$ component solid-solutions, which is 1167 K in this system. This serves as a proxy for the temperature where enthalpic effects in the competing solid-solution and ordered phases become important.

In Fig. 4, we see that intermetallics do not offer significant thermodynamic competition in the HfMoNbTiZr system; the binary intermetallics (in red text) all have formation energies more positive than -0.05 eV per atom, and there are no higher-component intermetallics. Out of all of the solid-solutions, MoTi is the only phase likely to pose a threat to HEA stability in the Hf–Mo–Nb–Ti–Zr system. Solid-solutions are stable across much of this system, indicated by the large number of blue marker labels, and three out of the four stable intermetallics contain Mo while the fourth, HfZr, has negligibly small formation energy. HfMoNbTiZr has the lowest formation energy in the entire five-component chemical space, and at the Mo melting temperature, has a sizable inverse hull energy of -0.05 eV per atom.

As the system is quenched, HfMoNbTiZr’s ‘critical adjacent phase’ temperature is 1167 K, meaning enthalpic effects do not become important until roughly 1700 K below Mo’s melting temperature. The HEA solid-solution is stable until only a few hundred Kelvin above room temperature as it has a ‘critical solid-solution’ temperature of 563 K. Additionally, the HEA solid-solution is only slightly metastable at room temperature with an energy above the hull of 12 meV per atom, a small energy value relative to the scale of metastability in quinary compounds²⁹. Altogether, these features suggest that HfMoNbTiZr is likely to persist as a metastable single solid-solution at room temperature.

In Fig. 4, we see that the HEA solid-solution initially decomposes into Zr and HfMoNbTi when it becomes unstable, indicated by the arrows extending from the pentagon at 563 K in Fig. 4. This means the quaternary HfMoNbTi solid-solution is more stable than the quinary HfMoNbTiZr alloy, suggesting that the addition of Zr to HfMoNbTi may give rise to a miscibility gap in the alloy at lower temperatures. Additionally, the quaternary HfMoNbTi solid-solution has the lowest formation energy in the system at 1167 K, further suggesting the addition of Zr to HfMoNbTi increases the energy of the solid-solution. Supplementary Video 1 can be referenced to watch the HfMoNbTiZr solid solution transition from stability to metastability at 563 K.

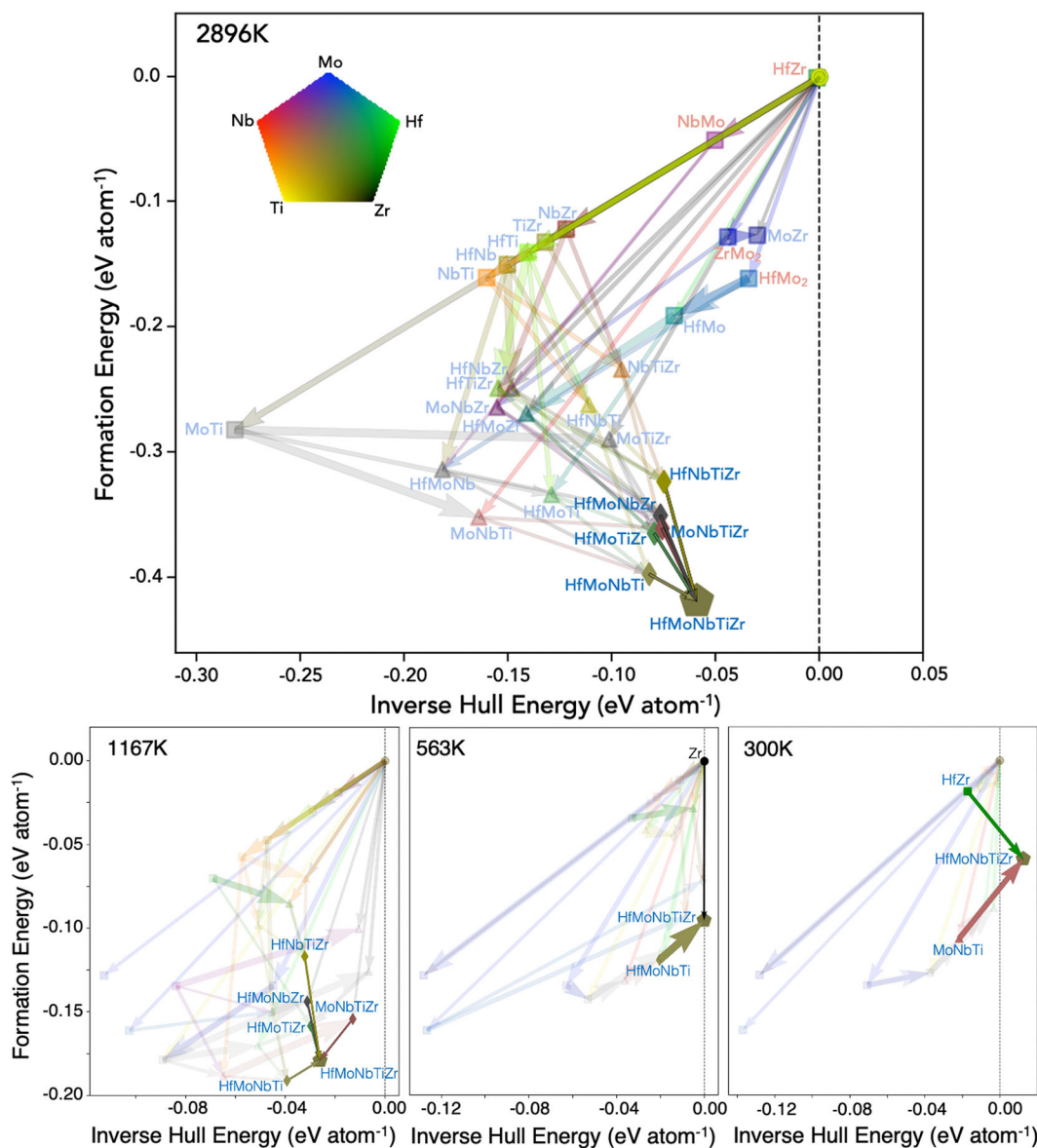


Fig. 4 Inverse hull web of HfMoNbTiZr. HfMoNbTiZr system at temperatures of 2896, 1167, 563, and 300 K. The top Inverse Hull Web is at 2896 K, the highest melting temperature in the Hf–Mo–Nb–Ti–Zr system, and the bottom left Inverse Hull Web is at 1167 K, HfMoNbTiZr’s ‘critical adjacent phase’ temperature. The bottom left Inverse Hull Web is at 563 K, HfMoNbTiZr’s ‘critical solid-solution’ temperature, and the bottom right Inverse Hull Web is at room temperature. We leave the single solid-solution and its hull reactants opaque, while we make all other phases partially transparent. A video of this Inverse Hull Web at decreasing temperatures from 2500 to 300 K can be found in Supplementary Video 1 and a tutorial of how to create this video can be found in Supplementary Data 1.

Our Inverse Hull Webs display the low critical temperatures, lack of energetically deep intermetallic phases, and low metastability of the HEA solid-solution at room temperature in the Hf–Mo–Nb–Ti–Zr system, allowing us to infer that this system is amenable to persist as a metastable single solid-solution HEA at ambient conditions. These stability relationships corroborate the experimental observations of Tseng et al of a room temperature solid-solution in HfMoNbTiZr, demonstrating the utility of our proposed diagrams.

Inverse hull web of an experimentally-observed multiphase HEA

Our Inverse Hull Webs can also be used to visualize features that may inhibit single solid-solution stability in HEAs. We demonstrate this with AlCrFeNi, a derivative of the CoCrFeMnNi Cantor alloy achieved by replacing Co and Mn with Al. The Cantor alloy was

one of the first HEAs found to exhibit a single solid-solution microstructure, however it was later discovered that the HEA solid-solution phase becomes metastable at around 800 °C^{18,19}. Chen et al found the AlCrFeNi alloy to be a phase separated AlNi B2 intermetallic and CrFe BCC solid-solution at room temperature after being cast through arc melting and remelted five times³⁸.

We show the AlCrFeNi Inverse Hull Web in Fig. 5 at 3853, 2180, 1650, and 300 K, corresponding to AlCrFeNi’s ‘critical adjacent phase’ temperature, Cr’s melting temperature, AlCrFeNi’s ‘critical solid-solution’ temperature, and room temperature. A visualization of phase stability in this system using traditional phase diagrams can be found in Supplementary Fig. 2, where we show a series of tetrahedral phase diagrams of the Al–Cr–Fe–Ni system at the four temperatures used in Fig. 5.

Figure 5 shows that Al–Ni intermetallics threaten HEA solid-solution stability in all alloy systems containing these elements. Al

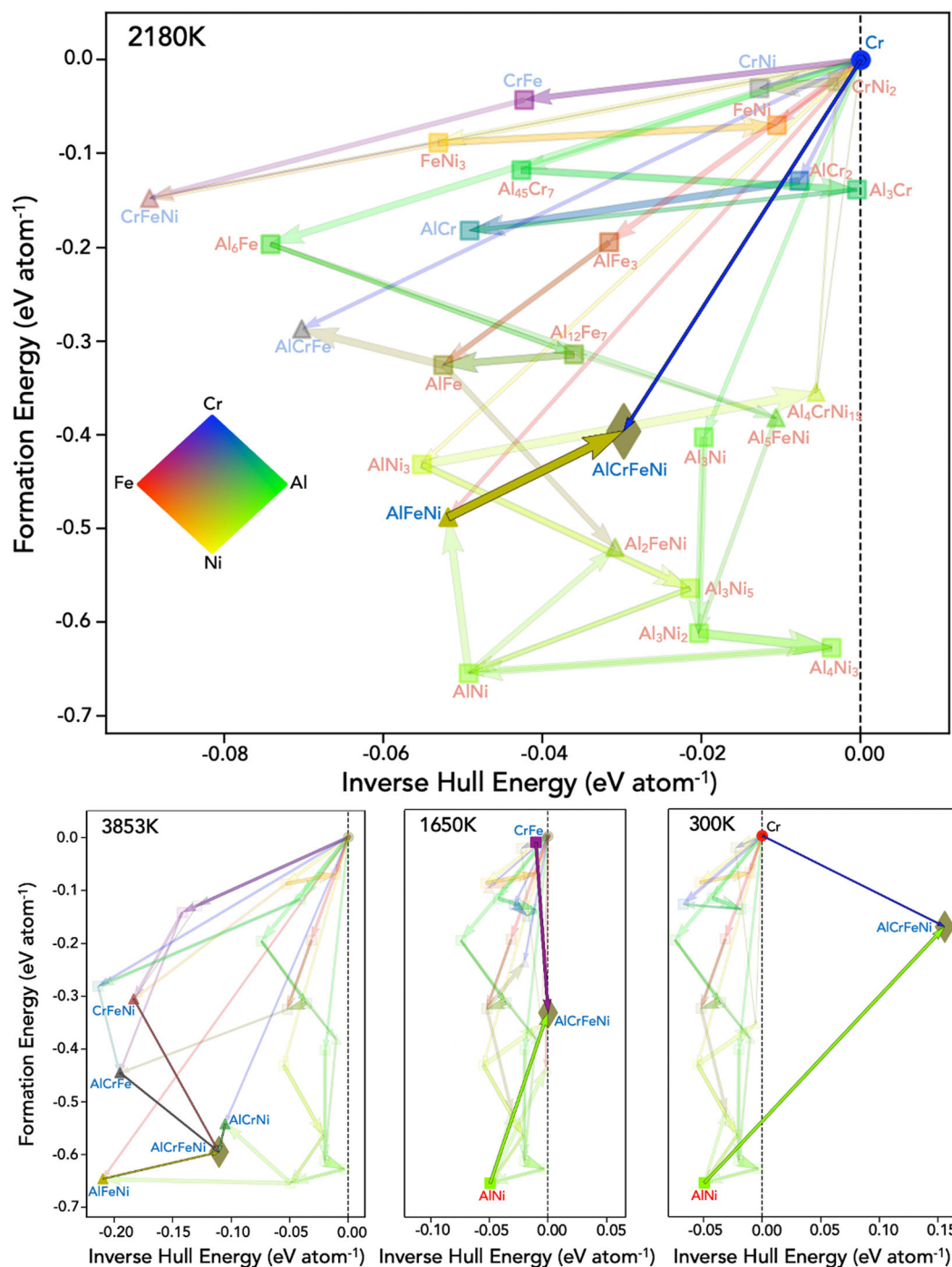


Fig. 5 Inverse hull web of AlCrFeNi. AlCrFeNi system at temperatures of 2180, 3853, 1650, and 300 K. The top Inverse Hull Web is at 2180 K, the highest melting temperature in the Al–Cr–Fe–Ni system, and the bottom left Inverse Hull Web is at 3853 K, AlCrFeNi’s ‘critical adjacent phase’ temperature. The bottom left Inverse Hull Web is at 1650 K, AlCrFeNi’s ‘critical solid-solution’ temperature, and the bottom right Inverse Hull Web is at room temperature. A video of this Inverse Hull Web at decreasing temperatures from 2500 to 300 K can be found in Supplementary Video 2.

–Ni intermetallics have very negative formation energies of -0.6 to -0.7 eV, as well as small inverse hull energies of -0.01 to -0.05 eV at all casting-relevant temperatures, which is visually apparent by the large number of green–yellow markers in the lower right of every Inverse Hull Web in Fig. 5. This suggests that the Al–Ni isopleth is littered with competing low-energy compounds.

Upon casting, the stability of the HEA solid-solution is immediately threatened by Al–Ni intermetallics. The highest

melting temperature in the Al–Cr–Fe–Ni system is 2180 K, while the ‘critical adjacent phase’ temperature is 3853 K. In this alloy, the ‘critical adjacent phase’ temperature is the lowest temperature where the four-component solid-solution’s hull reactants are each of the three-component solid-solutions, meaning below this temperature the single solid-solution begins to compete with either binary solid-solutions or ordered intermetallics. Figure 5 shows that the HEA solid-solution has a similar formation energy as Al–Ni intermetallics at 3853 K, suggesting that these intermetallics

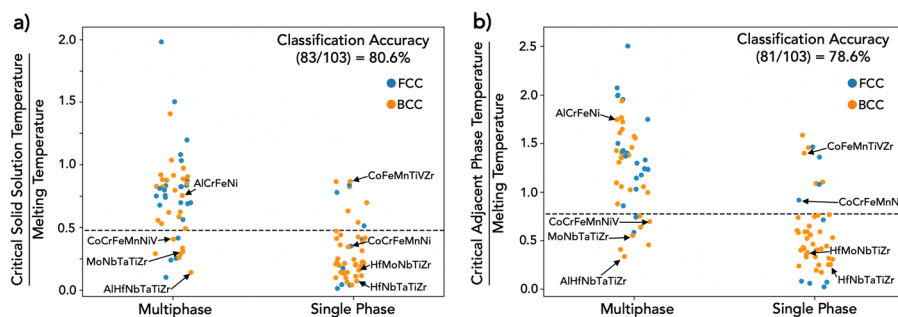


Fig. 6 Critical temperatures of 103 equimolar, as-cast HEAs. **a** ‘Critical solid-solution’ temperature of each HEA divided by the highest melting temperature of the pure elements in the HEA system. **b** ‘Critical adjacent phase’ temperature of each HEA divided by the highest melting temperature of the pure elements in the HEA system. Only FCC and BCC phases are considered, as the regular solution parameters in³³ are for FCC and BCC phases. Cutoff values of 0.48 and 0.78 were chosen in **(a, b)**, respectively, as these cutoff values result in the highest fraction of alloys being correctly classified as single or multiphase, 80.6 and 78.6%, respectively. A different choice of cutoff values would result in lower classification accuracies. Values for AlCrFeNi, CoCrFeMnNi, HfMoNbTiZr, HfNbTaTiZr, MoNbTaTiZr, AlHfNbTaTiZr, CoFeMnTiZr, and CoCrFeMnNiV are labeled with arrows. The critical temperatures of all 103 HEAs shown can be found in Supplementary Data 2.

would possess a large bulk driving force to nucleate at high temperatures, which would threaten the stability of an HEA solid-solution.

The HEA solid-solution in this system then becomes metastable at 1650, 600 K higher than in the Cantor alloy and more than 1000 K higher than in HfMoNbTiZr. Additionally, the HEA solid-solution is highly metastable at room temperature with an energy above the hull of 0.15 eV per atom, a large energy value relative to the scale of metastability in quaternary compounds, and more than 0.10 eV per atom more metastable than HfMoNbTiZr at room temperature²⁹. Supplementary Video 2 can be referenced to watch the AlCrFeNi solid solution transition from stability to metastability at 1650 K down to its high inverse hull energy at room temperature.

Altogether, AlCrFeNi’s high ‘critical adjacent phase’ temperature relative to its constituents’ melting temperatures, high ‘critical solid-solution’ temperature, and high metastability at room temperature are characteristic of phase-separating HEA systems. Even though this system is only a quaternary HEA, the threat posed by low-energy Al–Ni binary intermetallics should threaten other HEAs that contain these two elements. Our Inverse Hull Webs rationalize the experimental observations of Chen et al. of phase separation in this system into an AlNi intermetallic and a CrFe solid-solution.

Analysis of critical temperatures in HEAs

The critical solid solution and critical adjacent phase temperatures of an HEA are features that may be more broadly indicative of HEA solid-solution stability. We next calculate these critical temperatures for 103 equimolar, as-cast HEAs found in ref.³⁶ and use each temperature individually to classify the HEAs as single or multiphase. Here, a single cutoff value of the critical temperature is used to classify HEAs as either single or multiphase, where alloys with critical temperatures below the cutoff value are classified as single phase and alloys with critical temperatures above the cutoff value are classified as multiphase. We note that this is a one-parameter linear support vector classification, where a line is fit to distinguish between the two classes of HEA phase stability under consideration³⁹. Figure 6 shows the critical temperatures of each HEA divided by the highest melting temperature in the HEA system, along with the fraction of HEAs that were correctly classified as single or multiphase. Relative ‘critical solid-solution’ temperature is shown in Fig. 6a and relative ‘critical adjacent phase’ temperature is shown in Fig. 6b.

Figure 6 suggests that the single solid-solution needs to be stable at half of the casting temperature and entropic effects need to dominate down to 4/5 of the casting temperature for the HEA

to be a single solid-solution at room temperature. This can be seen in Fig. 6 as the cutoff value of relative ‘critical solid-solution’ temperature is 0.78 the cutoff value of relative ‘critical adjacent phase’ temperature is 0.48. AlCrFeNi and HfMoNbTiZr were correctly classified with both temperatures, and the Cantor alloy was as well.

Figure 6 shows that both ‘critical solid-solution’ temperature and ‘critical adjacent phase’ temperature are effective at distinguishing between single and multiphase HEAs, achieving classification accuracies of 80.6 and 78.6%, respectively, even when used in isolation and selecting a single cutoff value. This demonstrates the effectiveness of the critical temperatures in distinguishing between single and multiphase HEA compositions, suggesting that these temperatures may be valuable when used in a machine learning model aimed at predicting HEA phase stability^{40–44}. Machine learning models have been applied to predict HEA phase stability in the past, often using features such as the ideal mixing entropy, regular solution enthalpy, atomic size difference, and electronegativity difference of the HEA composition; these models are able to achieve classification accuracies > 80% by using several features in complex machine learning models, such as neural networks^{45–47}.

Our critical temperatures, by themselves, are able to achieve comparable classification performance as these machine-learning models, which demonstrates that the use of physically-motivated features directly relevant to HEA solid-solution stability may be more relevant in the prediction of HEA phase stability than sophisticated machine learning methods applied on less-relevant features⁴⁸. By including our critical temperature features as future machine-learning features, we anticipate that machine-learned classification performance can improve even further.

DISCUSSION

Our Inverse Hull Webs display both high-level trends in temperature-dependent phase stability, as well as precise details regarding the thermodynamic competition between compounds. Importantly, by displaying salient thermodynamic information in 2D for any *N*-component system, we overcome a major limitation of traditional phase diagrams for analyzing high-component systems—as shown here to rationalize solid-solution stability in HEAs. Regions of composition space that pose a threat to HEA solid-solution stability can be identified by compounds with very negative formation energies, such as Al–Ni intermetallics in the AlCrFeNi system. The thermodynamic incentive for an HEA to persist as a solid-solution or to decompose can be assessed by its temperature-dependent inverse hull energy. Altogether, these Inverse Hull Webs can serve as valuable tools to assist in the

guided discovery of experimentally-synthesizable disordered (or ordered) high-component materials.

Our analysis of single solid-solution stability in these high-entropy alloys further reveals two important features—the ‘critical solid-solution’ temperature and ‘critical adjacent phase’ temperature. ‘Critical solid-solution’ temperature is the lowest temperature where the HEA solid-solution is stable and thus estimates where the HEA solid-solution begins to decompose. ‘Critical adjacent phase’ temperature is the lowest temperature where the N -component HEA solid-solution’s hull reactants are each of the $(N-1)$ component solid-solutions, estimating where entropic effects no longer dominate. These features may illuminate which HEA compositions are likely to be found as a single solid-solution phase at room temperature and may be valuable features for a machine-learning model aimed at predicting single-phase HEA compositions.

Generally speaking, our Inverse Hull Webs offer a thermodynamic perspective that is complementary to the traditional representation of a convex hull. Typical phase diagrams visualize only the equilibrium phases at a given composition and do not provide formation energy or reaction energy information. Our Inverse Hull Webs reveal other important aspects of the thermodynamic landscape, such as convex hull depth, reaction driving forces, metastability, and the tendency for phase separation, all of which are difficult to ascertain from the traditional phase diagram. Even though our Inverse Hull Webs do not use barycentric composition axes, we are able to recover composition information by utilizing a variety of plot features, such as color, line width, and marker shape. We hope that by rethinking the classical approach to constructing phase diagrams, our work inspires the creation of yet-to-be-designed visualizations that can illuminate important trends in the *synthesis-structure-property-performance* relationships of advanced materials.

METHODS

Calculation of compound free energies

Intermetallic free energies were obtained from The Materials Project database³⁴ through the *pymatgen* Python package⁴⁹. Solid-solution free energies were calculated using a regular solution model as shown in Eq. 6, where N refers to the number of components, x_i refers to the mole fraction of the i^{th} element, and Ω_{ij} is the parameter that quantifies the interaction resulting from mixing the i^{th} and j^{th} elements.

$$\Delta G_{\text{mix}} = \sum_{i=1}^N \sum_{j>i}^N \Omega_{ij} x_i x_j + k_B T \sum_{i=1}^N x_i \ln(x_i) \quad (6)$$

Bokas et al. used DFT free energies of binary solid-solutions to fit a regular solution parameter Ω for each binary pair of elements out of 27 elements commonly used in HEAs, using the Special Quasirandom Structure (SQS) method to calculate the energy of solid-solution phases³³. A positive value of Ω corresponds to a binary alloy system that displays an isostructural miscibility gap, while a negative value of Ω corresponds to a binary system where mixing is enthalpically preferred. These regular solution parameters were used to calculate solid-solution free energies in our Inverse Hull Webs. The lower free energy of the FCC and BCC solid-solutions was found for each equimolar combination of elements in the chemical system being plotted. All compound free energies were referenced to the stable phases of the pure elements composing the compound. Formation and inverse hull energies were calculated using *pymatgen*⁴⁹. All Inverse Hull Webs were constructed using the *matplotlib* Python package⁵⁰.

DATA AVAILABILITY

A dataset of the critical temperatures used to create Fig. 6 can be found in Supplementary Data 2 as a csv file. Inverse Hull Webs of all 103 HEAs shown in Fig. 6 can be found in an online repository, https://www.dropbox.com/sh/0blhpbhu7o1510i/AADRKBI4WYAT3bvRqCW_w0Jya?dl=0. Each Inverse Hull Web in this repository follows a similar format to Figs. 4 and 5, where a large Inverse Hull Web is shown at the highest melting temperature of the pure elements and three smaller Inverse Hull

Webs are shown at the alloy’s ‘critical adjacent phase’ temperature, ‘critical solid solution’ temperature, and room temperature.

CODE AVAILABILITY

The code used to obtain the free energy of phases and construct Inverse Hull Webs can be found in Supplementary Data 1. Python classes to build and construct Inverse Hull Webs can be found in *inverse_hull_web.py* in Supplementary Data 1 and *ihw_tutorial.py* in Supplementary Data 1 walks through the calculation of solid solution free energies and subsequent Inverse Hull Web Construction.

Received: 10 May 2021; Accepted: 19 August 2021;
Published online: 24 September 2021

REFERENCES

- Li, Z., Zhao, S., Ritchie, R. O. & Meyers, M. A. Mechanical properties of high-entropy alloys with emphasis on face-centered cubic alloys. *Prog. Mater. Sci.* **102**, 296–345 (2019).
- Li, Z. & Raabe, D. Strong and ductile non-equiatomic high-entropy alloys: design, processing, microstructure, and mechanical properties. *JOM* **69**, 2099–2106 (2017).
- Fu, Z. et al. A high-entropy alloy with hierarchical nanoprecipitates and ultrahigh strength. *Sci. Adv.* **4**, 1–9 (2018).
- George, E. P., Curtin, W. A. & Tسان, C. C. High entropy alloys: a focused review of mechanical properties and deformation mechanisms. *Acta Mater.* **188**, 435–474 (2020).
- Li, Z., Pradeep, K. G., Deng, Y., Raabe, D. & Tسان, C. C. Metastable high-entropy dual-phase alloys overcome the strength-ductility trade-off. *Nature* **534**, 227–230 (2016).
- Qiu, Y., Thomas, S., Gibson, M. A., Fraser, H. L. & Birbilis, N. Corrosion of high entropy alloys. *npj Mater. Degrad.* **1**, 1–17 (2017).
- Shi, Y., Yang, B. & Liaw, P. K. Corrosion-resistant high-entropy alloys: a review. *Metals* **7**, 1–18 (2017).
- Fu, X., Schuh, C. A. & Olivetti, E. A. Materials selection considerations for high entropy alloys. *Scr. Mater.* **138**, 145–150 (2017).
- Oh, H. S. et al. Engineering atomic-level complexity in high-entropy and complex concentrated alloys. *Nat. Commun.* **10**, 1–8 (2019).
- Oses, C., Toher, C. & Curtarolo, S. High-entropy ceramics. *Nat. Rev. Mater.* **5**, 295–309 (2020).
- Rost, C. M. et al. Entropy-stabilized oxides. *Nat. Commun.* **6**, 1–8 (2015).
- Meisenheimer, P. B., Kratochil, T. J. & Heron, J. T. Giant enhancement of exchange coupling in entropy-stabilized oxide heterostructures. *Sci. Rep.* **7**, 3–8 (2017).
- Meisenheimer, P. B. et al. Magnetic frustration control through tunable stereochemically driven disorder in entropy-stabilized oxides. *Phys. Rev. Mater.* **3**, 1–9 (2019).
- Deng, Z. et al. Semiconducting high-entropy chalcogenide alloys with ambi-ionic entropy stabilization and ambipolar doping. *Chem. Mater.* **32**, 6070–6077 (2020).
- Luo, Y. et al. High thermoelectric performance in the new cubic semiconductor AgSbSbSe₃ by high-entropy engineering. *J. Am. Chem. Soc.* **142**, 15187–15198 (2020).
- Lun, Z. et al. Cation-disordered rocksalt-type high-entropy cathodes for Li-ion batteries. *Nat. Mater.* **20**, 214–221 (2020).
- Wang, Q. et al. Multi-anionic and -cationic compounds: new high entropy materials for advanced Li-ion batteries. *Energy Environ. Sci.* **12**, 2433–2442 (2019).
- George, E. P., Raabe, D. & Ritchie, R. O. High-entropy alloys. *Nat. Rev. Mater.* **4**, 515–534 (2019).
- Cantor, B., Chang, I. T. H., Knight, P. & Vincent, A. J. B. Microstructural development in equiatomic multicomponent alloys. *Mater. Sci. Eng., A* **375**, 213–218 (2004).
- Yeh, J. W. et al. Nanostructured high-entropy alloys with multiple principal elements: novel alloy design concepts and outcomes. *Adv. Eng. Mater.* **6**, 299–303 (2004).
- Toher, C., Oses, C., Hicks, D. & Curtarolo, S. Unavoidable disorder and entropy in multi-component systems. *npj Comput. Mater.* **5**, 10–12 (2019).
- Wang, Y. et al. Computation of entropies and phase equilibria in refractory V–Nb–Mo–Ta–W high-entropy alloys. *Acta Mater.* **143**, 88–101 (2018).
- Miracle, D. B. & Senkov, O. N. A critical review of high entropy alloys and related concepts. *Acta Mater.* **122**, 448–511 (2017).
- Senay, H., & Ignatius, E. *Rules and Principles of Scientific Data Visualization* (Institute for Information Science and Technology, Department of Electrical Engineering and Computer Science, School of Engineering and Applied Science, George Washington University, 1990).

25. Maltese, A., Harsh, J. & Svetina, D. Data visualization literacy: investigating data interpretation along the novice-expert continuum. *J. Coll. Sci.* **45**, 84 (2015).
26. Hegde, V. I., Aykol, M., Kirkin, S. & Wolverton, C. The phase stability network of all inorganic materials. *Sci. Adv.* **6**, 1–6 (2020).
27. Aykol, M. et al. Network analysis of synthesizable materials discovery. *Nat. Commun.* **10**, 1–7 (2019).
28. Gibbs, J. W. On the equilibrium of heterogeneous substances. *Trans. Conn. Acad.* **3**, 343–524 (1878).
29. Sun, W. et al. The thermodynamic scale of inorganic crystalline metastability. *Sci. Adv.* <https://doi.org/10.1126/sciadv.1600225> (2016).
30. Gehlenborg, N. & Wong, B. Points of view: mapping quantitative data to color. *Nat. Methods* **9**, 769 (2012).
31. Waters, M. J., Walker, J. M., Nelson, C. T., Joester, D. & Rondinelli, J. M. Exploiting colorimetry for fidelity in data visualization. *Chem. Mater.* **32**, 5455–5460 (2020).
32. Meyer, M., Barr, A., Lee, H. & Desbrun, M. Generalized barycentric coordinates on irregular polygons. *J. Graph. Tools* **7**, 13–22 (2002).
33. Bokas, G. B., et al. Unveiling the thermodynamic driving forces for high entropy alloys formation through big data ab initio analysis. *Scr. Mater.* <https://doi.org/10.1016/j.scriptamat.2021.114000> (2021).
34. Jain, A. et al. Commentary: The materials project: a materials genome approach to accelerating materials innovation. *APL Mater.* <https://doi.org/10.1063/1.4812323> (2013).
35. Fitzgerald, R. K. & Verhoek, F. H. The law of Dulong and Petit. *J. Chem. Educ.* **37**, 545 (1960).
36. Qi, J., Cheung, A. M. & Poon, S. J. High entropy alloys mined from binary phase diagrams. *Sci. Rep.* **9**, 1–10 (2019).
37. Tseng, K. K. et al. Effects of Mo, Nb, Ta, Ti, and Zr on mechanical properties of equiatomic Hf–Mo–Nb–Ta–Ti–Zr alloys. *Entropy* **21**, 1–14 (2019).
38. Chen, X. et al. Effects of aluminum on microstructure and compressive properties of Al–Cr–Fe–Ni eutectic multi-component alloys. *Mat. Sci. Eng., A* **681**, 25–31 (2017).
39. Cortes, C. & Vapnik, V. Support-vector networks. *Mach. Learn.* **20**, 273–297 (1995).
40. Jain, A., Hautier, G., Ong, S. P. & Persson, K. New opportunities for materials informatics: resources and data mining techniques for uncovering hidden relationships. *J. Mater. Res.* **31**, 977–994 (2016).
41. Ong, S. P. Accelerating materials science with high-throughput computations and machine learning. *Comput. Mater. Sci.* **161**, 143–150 (2019).
42. De Breuck, P. P., Hautier, G. & Rignanese, G. M. Materials property prediction for limited datasets enabled by feature selection and joint learning with MODNet. *npj Comput. Mater.* **7**, 1–8 (2021).
43. Bartel, C. J. et al. New tolerance factor to predict the stability of perovskite oxides and halides. *Sci. Adv.* <https://doi.org/10.1126/sciadv.aav0693> (2018).
44. Kaufmann, K. et al. Discovery of high-entropy ceramics via machine learning. *npj Comput. Mater.* **6**, 1–9 (2020).
45. Zhang, Y. et al. Phase prediction in high entropy alloys with a rational selection of materials descriptors and machine learning models. *Acta Mater.* **185**, 528–539 (2020).
46. Zhou, Z. et al. Machine learning guided appraisal and exploration of phase design for high entropy alloys. *npj Comput. Mater.* **5**, 1–9 (2019).
47. Huang, W., Martin, P. & Zhuang, H. L. Machine-learning phase prediction of high-entropy alloys. *Acta Mater.* **169**, 225–236 (2019).
48. Ghiringhelli, L. M., Vybiral, J., Levchenko, S. V., Draxl, C., & Scheffler, M. Big data of materials science: critical role of the descriptor. *Phys. Rev. Lett.* <https://doi.org/10.1103/PhysRevLett.114.105503> (2015).
49. Ong, S. P. et al. Python Materials Genomics (pymatgen): a robust, open-source python library for materials analysis. *Comput. Mater. Sci.* **68**, 314–319 (2013).

50. Hunter, J. D. Matplotlib: a 2D graphics environment. *Comput. Sci. Eng.* **9**, 90–95 (2007).

ACKNOWLEDGEMENTS

This work by D.N.E., J.C., and W.S. was supported by the U.S. Department of Energy (DOE), Office of Science, Basic Energy Sciences (BES), under Award #DE-SC0021130. The work by G.B., W.C. and G.H. was funded by the Walloon Region under the agreement no. 1610154- EntroTough in the context of the 2016 Wallinnov call. Computational resources were provided by the supercomputing facilities of the UCLouvain and the Consortium des Equipements de Calcul Intensif (CECI) en Federation Wallonie Bruxelles, funded by the Fonds de la Recherche Scientifique de Belgique (FNRS).

AUTHOR CONTRIBUTIONS

J.C. and W.S. conceived the original research idea. D.N.E developed and applied the visualization to HEA systems and wrote the manuscript with feedback from W.S. G.B., W.C. and G.H. calculated the regular solution parameters used in the thermodynamic model. All authors contributed to revising the paper.

COMPETING INTERESTS

The authors declare no competing interests.

ADDITIONAL INFORMATION

Supplementary information The online version contains supplementary material available at <https://doi.org/10.1038/s41524-021-00626-1>.

Correspondence and requests for materials should be addressed to Wenhao Sun.

Reprints and permission information is available at <http://www.nature.com/reprints>

Publisher's note Springer Nature remains neutral with regard to jurisdictional claims in published maps and institutional affiliations.



Open Access This article is licensed under a Creative Commons Attribution 4.0 International License, which permits use, sharing, adaptation, distribution and reproduction in any medium or format, as long as you give appropriate credit to the original author(s) and the source, provide a link to the Creative Commons license, and indicate if changes were made. The images or other third party material in this article are included in the article's Creative Commons license, unless indicated otherwise in a credit line to the material. If material is not included in the article's Creative Commons license and your intended use is not permitted by statutory regulation or exceeds the permitted use, you will need to obtain permission directly from the copyright holder. To view a copy of this license, visit <http://creativecommons.org/licenses/by/4.0/>.

© The Author(s) 2021